remote sensing

MDPI

Article

A Novel Method for Layover Detection in Mountainous Areas with SAR Images

Lin Wu [1,2,3,4], Hongxia Wang [1,3,4], Yuan Li [1,3,4,5], Zhengwei Guo [1,3,4,*] and Ning Li [1,3,4]

1 College of Computer and Information Engineering, Henan University, Kaifeng 475004, China; henuwl@henu.edu.cn (L.W.); whx@henu.edu.cn (H.W.); liyuan_960423@vip.henu.edu.cn (Y.L.); hedalining@henu.edu.cn (N.L.)
2 College of Geography and Environmental Science, Henan University, Kaifeng 475004, China
3 Henan Engineering Research Center of Intelligent Technology and Application, Henan University, Kaifeng 475000, China
4 Key Laboratory of Big Data Analysis and Processing, Henan University, Kaifeng 475004, China
5 School of Information and Electronic Engineering, Shangqiu Institute of Technology, Shangqiu 476000, China
* Correspondence: gzw@henu.edu.cn

Abstract: It is well known that there are geometric distortions in synthetic aperture radar (SAR) images when the terrain undulates. Layover is the most common one, which brings challenges to the application of SAR remote sensing. This study proposes a novel detection method that is mainly aimed at the layover caused by mountains and can be performed with only medium-resolution SAR images and no other auxiliary data. The detection includes the following four stages: initial processing, difference image calculation and rough and fine layover detection. Initial processing mainly obtains the potential layover areas, which are mixed with the built-up areas after classification. Additionally, according to the analysis of the backscatter coefficient (BC) of various ground objects with different polarization images, the layover areas are detected step-by-step from the mixed areas, in which the region-based FCM segmentation algorithm and spatial relationship criteria are used. Taking the Danjiangkou Reservoir area as the study area, the relevant experiments with Sentinel-1A SAR images were conducted. The quantitative analysis of detection results adopted the figure of merit (*FoM*), and the highest accuracy was up to 87.6% of one selected validation region. Experiments in the South Taihang area also showed the satisfactory effect of layover detection, and the values of *FoM* were all above 85%. These results show that the proposed method can do well in the layover detection caused by mountains. Its simplicity and effectiveness are helpful in removing the influence of layover on SAR image applications to a certain extent and improving the development of SAR remote sensing technology.

Keywords: layover detection; backscatter coefficient analysis; undulating terrain; SAR image; medium resolution

check for updates

Citation: Wu, L.; Wang, H.; Li, Y.; Guo, Z.; Li, N. A Novel Method for Layover Detection in Mountainous Areas with SAR Images. *Remote Sens.* **2021**, *13*, 4882. https://doi.org/10.3390/rs13234882

Academic Editors: Ali Khenchaf and Jean-Christophe Cexus

Received: 29 October 2021
Accepted: 30 November 2021
Published: 1 December 2021

1. Introduction

As a typical active microwave imaging sensor, synthetic aperture radar (SAR) has the abilities of all-day and all-weather observation [1]. It has been broadly applied in many fields, such as natural resources surveys, topographic mapping, ground object extraction and disaster monitoring [2]. Decision tree (DR), support vector machine (SVM), Markov random field (MRF), deep learning and other artificial intelligence technologies have been introduced into the processing and analysis of remote sensing information [3–8].

Considering availability and universality, SAR images with medium resolution are still the most widely used images in large-scale remote sensing monitoring at present. Table 1 shows the information of common space-borne SAR images [9]. The Sentinel-1 satellite is one of the Earth observation satellites of the European Space Agency's Copernicus initiative, launched on 3 April 2014. With the advantage of large range covering, long time-series image resources and a convenient data service, SAR images from Sentinel-1A are being employed in more and more applications [10].

Table 1. The information of common spaceborne SAR images.

SAR Sensor Platform	Mode	Swath (km^2)	Resolution (m)
Sentinel-1A/B	TOPS	250	20
GF-3	Standard strip	130	25
TerraSAR-X	ScanSAR	100	16
ALOS-2	ScanSAR	350	25
COSMO-SkyMed	ScanSAR	100	30

Due to the side-looking and range imaging characteristics of SAR sensors [11], geometric distortions are inevitable in high-relief areas. Layover is the common distortion phenomenon, which will greatly limit the application of SAR images. Especially in mountainous areas, the information in a SAR image is inconsistent with the real state of the ground objects. It is of great significance to detect layover, which can effectively avoid the inaccuracy of SAR data.

Thus far, there has not been much research about layover detection in SAR images. Layover detection methods are mainly for the application of InSAR technology in the early stage. Interferogram analysis is often used as the basic means of detection. Gatelli et al. [12] used the different frequencies of the interferon spectrum to identify the areas of layover and non-layover during InSAR processing. Gini et al. [13] illustrated spectral estimation techniques to overcome the layover problem during the processing of multichannel InSAR data. Eineder et al. [14] adopted a maximum likelihood estimation method to fuse ascending and descending interferograms into a fine digital elevation model (DEM), in which the errors caused by layover and shadow were dealt with. Cai et al. [15] proposed a signal number estimation method based on the interferometric signal autocorrelation matrix to distinguish layover and shadow from normal InSAR fields. Ren et al. [16] used the coherent coefficient map and the interferometric amplitude to avoid the impact of layover and shadow on phase unwrapping. Du et al. [17] proposed a method of layover and shadow detection based on local frequency estimation, amplitude division and morphological processing to restore phase continuity.

The relationship between the SAR look angle and the land slope is another way to detect layover. To calculate these figures, information on the position of the sensor and DEM data are usually required. Guindon et al. [18] detected layover by computing the magnitude of the SAR look angle and slant range for each DEM sub-sample. Zhang et al. [19] proposed a layover area determination method based on the relationship between the look angle and the slope angle in the range direction. Kakooei et al. [20] fused multi-temporal images and SRTM DEM data to detect foreshortening areas using the Google Earth Engine (GEE) platform. Zhang et al. [21] used the geometric model of SAR imaging and the morphological method to identify the layover and shadow areas caused by mountains. Wang et al. [22] used the rational function model (RFM) to determine the layover range.

In the above studies, the following issues should be noted: (1) Simulated data are often used in the experiments [2,4–10]; thus, the detection result will be affected once the ideal data are replaced with the real SAR image. (2) DEM data are the essential auxiliary data [3,5,7–10], and detection cannot be performed while the DEM of the study area is absent. (3) More restrictions on the SAR data for detection are required. For example, two coherent SAR images are required [1–6], full polarized or high-resolution SAR images [8,11] are needed, etc. (4) No quantitative results are given; therefore, it is difficult to conduct comparative analysis.

Considering the foregoing, a novel method based on the analysis of the backscatter coefficient (BC) is proposed for layover detection, which aims to simplify the data requirements. Sentinel-1A SAR images were used. Several experiments in the Danjiangkou Reservoir area and South Taihang area were conducted, and the detection results of layover areas caused by mountains were highly consistent with the real ground situation. Additionally, the highest value of *FoM* was up to 87.6%. The main contributions of this study are as follows:

- Layover can be distinguished from built-up areas by a BC difference between the VV and VH images, although they are visually similar.
- A medium-resolution SAR image can do well in layover detection. Thus, some research can remove the dependence on a high-resolution image, especially in the absence of it.

The rest of this paper is arranged as follows. A characteristics analysis in relation to SAR images with layover is discussed in Section 2. The details of the proposed method are described in Section 3. In Section 4, the experimental results and analysis are provided. In Section 5, some conclusions are drawn.

2. Geometry Model and BC Analysis in Mountainous Areas

2.1. Geometry Model

Layover is an extreme case of foreshortening, and both of them are geometric distortions that occur in rugged mountainous areas. Figure 1 shows the imaging geometry of a SAR sensor.

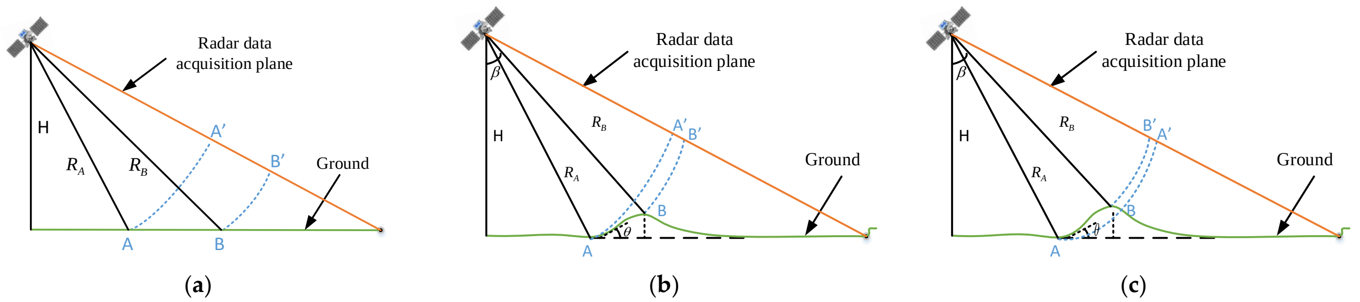

Figure 1. Sketch of SAR imaging: (**a**) that of the flat area; (**b**) foreshortening in mountainous area; (**c**) layover in mountainous area.

In the flat area, shown in Figure 1a, the slant range distances of ground targets A and B from the sensor are R_A and R_B, respectively, and their projections on an acquisition plane are A′ and B′, respectively. There is a monotonic relationship between AB and A′B′.

When the SAR signal reaches a mountainous area that is less steep, it will generate a foreshortening phenomenon, as shown in Figure 1b. AB is the fore slope, and the slant range R_B is shorter than R_A due to the existence of θ. The echo of AB is concentrated on A′B′, and the signal is compressed compared with that of a flat area. Therefore, an unusually high BC occurs here, and the information of the SAR image is incorrect.

Once the slop angle is large, the foreshortening phenomenon will worsen; that is, layover, as shown in Figure 1c. R_B is shorter than that in Figure 1b, and B′, the echo of B, reaches the acquisition plane before A′, thus a top–bottom inversion occurs. These are the typical characteristics of layover. However, as with foreshortening, there is still a high BC in the layover area.

As the proposed method is suitable for both, foreshortening and layover are collectively referred to as layover for convenience in this study, just as they are in other similar studies.

2.2. BC Analysis

In general, common land cover includes built-up areas, water, woodland and farmland. The diversity in surface roughness, soil humidity and object structure is recorded using SAR sensors with different values, which can be used for the recognition of ground objects. For one single image, the interpretation usually depends on the BC value, which is calculated from the amplitude data.

The BC value of each pixel in a SAR image is calculated using Formula (1).

$$\sigma^{o}(i,j) = 10 \cdot \lg\left(\frac{\left|DN_{i,j}\right|^{2}}{A_{\sigma}^{2}}\right) \tag{1}$$

where σ^{o} is the BC value, DN is the value of pixel, A_{σ} is the calibration parameter and i and j represent the ith row and jth column, respectively.

Some researchers have studied the BC values of different types of land cover [23–25], and the approximate ranges of these values are shown in Table 2, which are the important basis for many classification and recognition methods based on threshold. Among all the ground objects, water has the lowest value owing to the spectacular reflection. Built-up areas have the highest value due to the double-bounce scattering of right-angle structures. Additionally, the values of woodland and farmland are in the middle range, which will change slightly with the growth of vegetation.

Table 2. BC ranges of different types of land cover.

Category	Built-Up Areas	Vegetation	Farmland	Water
BC	>−13 dB	(−10 dB)–(−15 dB)	(−8 dB)–(−18 dB)	<−18 dB

With the same method, the BC value of layover can be obtained from several SAR images. We randomly select ten samples of layover areas 7 × 7 pixels in size, calculate the BC using Formula (1), and the average of these values is considered as the BC value of layover. The BC values of the samples are all no less than −8 dB, which is similar to those of the built-up area, and most of them are higher than those of the built-up area. The high BC of layover is generated because the echo of multiple ground targets is compressed to a few pixels. Therefore, the layover detection based on the analysis of BC is practicable.

As we all know, the building density of cities and suburbs is different. In a bustling city, there are many buildings crowded in a small space, especially in the case of high-rise buildings. Additionally, few large tracts of other ground objects will be there, such as water, woodland and farmland. However, suburbia and the countryside are another situation. Farmland occupies most of the land. Although there are also residential houses, they are generally low in height and sparse in distribution and are often surrounded by farmland. Figure 2 shows the common distribution of built-up areas in cities and suburbs.

(**a**) (**b**)

Figure 2. Distribution of built-up areas in cities and suburbs: (**a**) city; (**b**) suburb.

In the city, there are more buildings with right-angled structures, which are prone to double-bounce scattering. That is the main reason for the high value of BC there. In this study, these high-density built-up areas (as shown in Figure 2a) are called "Dense building areas", while low-density areas (as shown in Figure 2b) are called "Sparse building areas".

However, it should be noted that the BC of the built-up areas shown in Table 1 is a general range, and there will be discrepancies for the different polarization images [26].

The six images in Figure 3 show the characteristics of Dense building areas, Sparse building areas and layover areas in VV and VH modes. It is visible from Figure 3a,b that Dense building areas appear brighter in a VV image. That is because the SAR sensor is more sensitive to double-bounce scattering in the co-polarized mode than in the cross-polarized mode. Therefore, the BC of Dense building areas is higher in a VV image than that in a VH image. However, this does not happen in Sparse building areas and layover areas, as shown in Figure 3c–f. In both of the two types of polarization SAR image, the BC of Sparse building areas remains lower, while that of layover areas is higher.

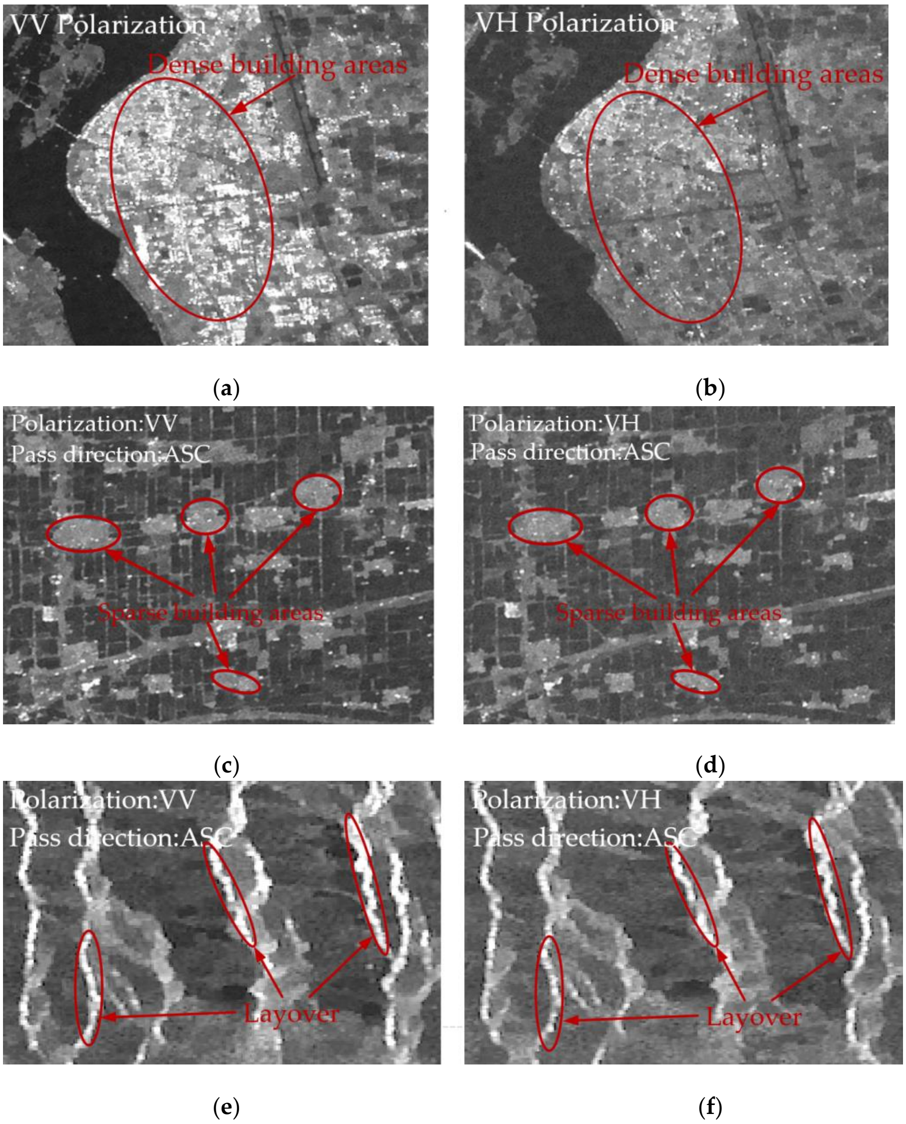

Figure 3. VV and VH images of three types of areas: (**a**) VV image of Dense building areas; (**b**) VH image of Dense building areas; (**c**) VV image of Sparse building areas; (**d**) VH image of Sparse building areas; (**e**) VV image of layover areas; (**f**) VH image of layover areas.

In order to quantify the difference discussed above, the BC of three types of areas was calculated using Formula (1). Every value in Table 3 is the average of the BC values obtained from 30 samples in the corresponding areas that are 7×7 pixels in size. It can be seen that these values are consistent with the visual characteristics shown in Figure 3.

Table 3. Average BC of three types of areas in different polarization SAR images.

	Dense Building Areas	Sparse Building Areas	Layover Areas
VV image	−1.98 dB	−8.89 dB	−5.8 dB
VH image	−7.34 dB	−8.42 dB	−6.01 dB

In short, layover areas are similar to the built-up areas in terms of BC but are closer to Sparse building areas than Dense building areas in terms of the difference image between the VV and VH images. The BC values of the layover areas and Sparse building areas almost remain unchanged in the two types of polarization image, but there is a greater difference between them in the Dense building areas. Based on this, Dense building areas can be extracted from built-up areas. Additionally, then, the spatial relationship around built-up areas is used to further detect layover areas.

3. Proposed Method for Layover Detection

The whole process of the proposed method is depicted in Figure 4. This method includes the following four stages: initial processing, difference image calculation, rough and fine layover detection. The initial processing obtains the potential areas with layover by image classification. According to the BC analysis in Section 2.2, layover areas will be misclassified as built-up areas, but the characteristics of them are not completely alike in different polarization modes and spatial relationships. Then, the layover areas can be extracted using a "Rough-Fine" two-step detection method based on the difference image of built-up areas.

3.1. Initial Processing

The recognition of common land cover is the prerequisite for layover detection. Generally, any SAR image can be used. However, many ground objects change seasonally. For example, the area of water change rises and falls with the influence of rainfall and other factors, and crops change in height or shape with their growth. For a better recognition result, a more suitable SAR image and an efficient classification algorithm should be selected with some effort.

Time series SAR images with different polarization modes throughout a year should be analyzed. According to Formula (1), the BC of various ground objects could be obtained. The temporal variation of these values was analyzed. The deviation of different objects in one image was the key point to be considered. The selection of the image for classification depended on the result of a standard deviation calculation. At the same time, the official land use data [27] or field survey data could be used as a reference. Owing to the built-up areas that are more prominent in VV mode, the optimal image was preferred to VV images.

As for the classification of algorithms, although deep learning, neural networks and other methods have achieved a lot in SAR applications, there are too few public sample sets available for layover detection. Therefore, the traditional algorithms were taken into account in this method. The OGMRF-RC (object-based Gaussian–Markov random field with regional coefficient) [28] algorithm, an object-oriented probabilistic graphic model, has a strong anti-noise ability due to the utilization of super-pixel and spatial context information. Experiments show that, compared with K-means, fuzzy C-means (FCM) and MRF algorithms, the OGMRF-RC algorithm has the best classification effect.

For a SAR image, suppose $R = \{r_1, r_2, \ldots, r_N\}$ is the set of regions after super-pixel segmentation and N is the number of regions. The fields $Y = \{y_1, y_2, \ldots, y_\mathrm{n}\}$ and $X = \{x_1, x_2, \ldots, x_\mathrm{n}\}$ represent the feature information and category label of each region, respectively, called the feature field and label field.

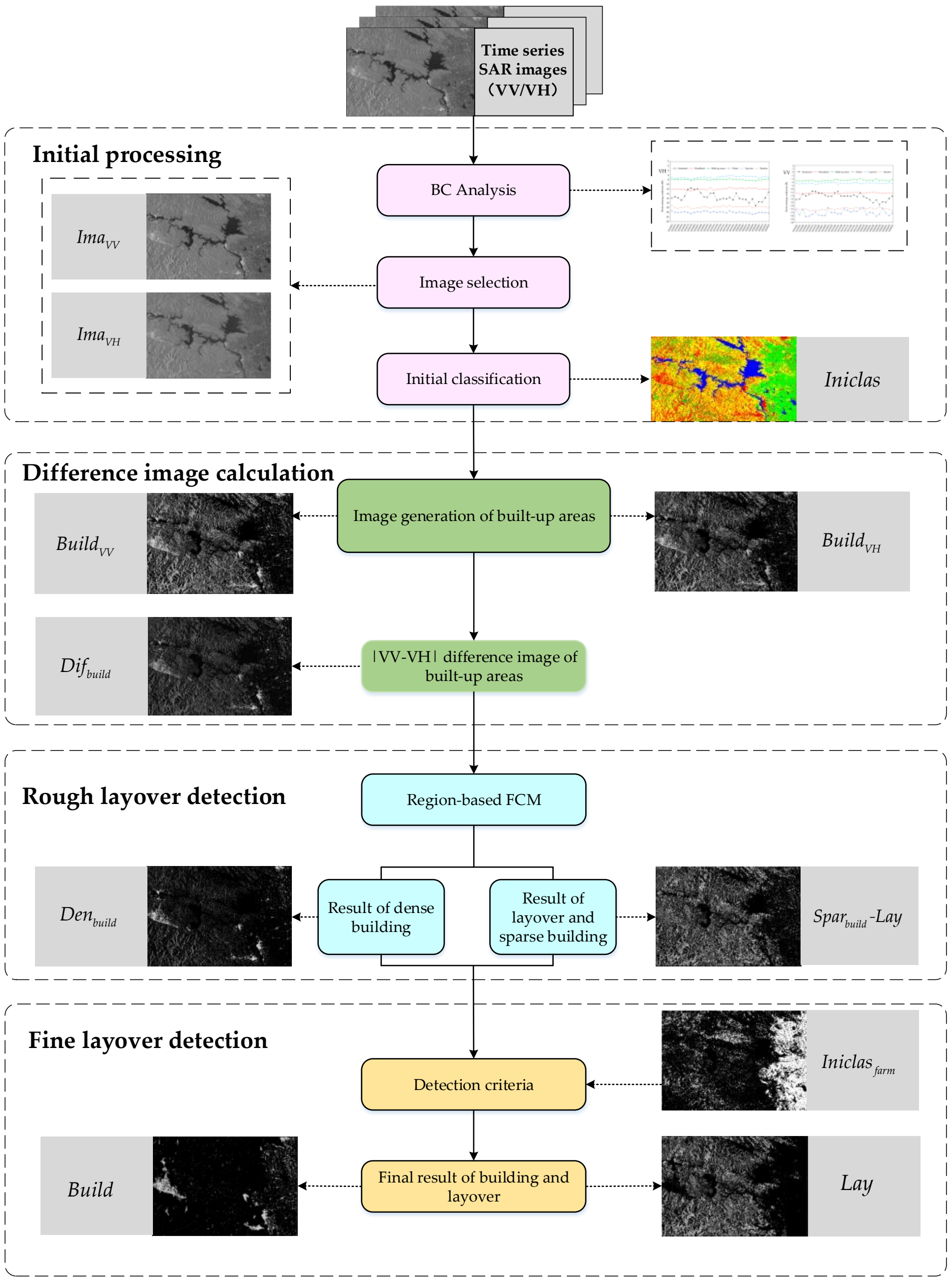

Figure 4. Flow chart of proposed method for layover detection.

The objective function of the OGMRF-RC algorithm is shown in Formulas (2) and (3).

$$x^* = Argmin\left\{ \frac{1}{2}\log(2\pi{\sigma_h}^2) + \frac{(y_i - \mu_h)^2}{2\sigma_h} + \sum_{r_j \in N_{r_i}} V(x_i, x_j) \right\} \tag{2}$$

$$V(x_i, x_j) = \begin{cases} -\beta, x_i = x_j \\ \beta, x_i \neq x_j \end{cases} \tag{3}$$

where h is the category of region r_i, and ${\sigma_h}^2$ and μ_h are the feature parameters representing the regional variance and regional meaning of category h. N_{r_i} is the neighborhood of region r_i, $V(x_i, x_j)$ is the potential energy function and β is the potential energy parameter.

This initial processing was preparation for layover detection. The classification of the selected image meant that woodland, farmland, water and built-up areas could be recognized, and layover areas were included in the built-up areas due to their similar BC values. The subsequent processing stages will extract the layover areas from them.

3.2. Difference Image Calculation

After this initial processing, all areas with characteristics similar to the built-up areas can be obtained. These areas were defined as the following three types in Section 2.2: Dense building areas, Sparse building areas and layover areas. This stage calculates the difference image using the two polarization images of VV and VH, which removes most of the Dense building areas.

Suppose $Iniclas$ denotes the classification result, and $Iniclas_{build}$ denotes the built-up areas in $Iniclas$. $Iniclas_{VV}$ and $Iniclas_{VH}$ represent the VV and VH images of the selected SAR image, respectively. $Build_{VV}$ and $Build_{VH}$ are the images of built-up areas with different polarization modes, calculated using Formulas (4) and (5).

$$Build_{VV} = Iniclas_{Build} \cap Ima_{VV} \tag{4}$$

$$Build_{VH} = Iniclas_{Build} \cap Ima_{VH} \tag{5}$$

Then, the difference image of built-up areas, Dif_{Build}, can be calculated using Formula (6).

$$Dif_{Build} = |Build_{VV} - Build_{VH}| \tag{6}$$

3.3. Rough Layover Detection

It is known from Table 3 that the BC values of Dense building areas are significantly different in VV and VH images. This difference is strengthened in Dif_{Build}. While the BC values of Sparse building areas and layover areas are similar, the information of the two types of areas is weak in Dif_{Build}. In this way, it is easy to classify the built-up areas into two categories using a segmentation algorithm. One is Dense building areas, denoted as Den_{Build}, and another is Sparse building areas and layover areas, denoted as $Spar_{Build}-Lay$.

The region-based fuzzy C-means (FCM) [29] algorithm was adopted to segment Dif_{Build} to extract Den_{Build}. Super-pixel is the basic processing unit in this algorithm, which can partly restrain the speckle noise of the SAR image. Additionally, the region set of super-pixel was acquired using the simple linear iterative clustering (SLIC) method [30–32] due to its convenience and speed.

The region set of Dif_{Build} is $X = \{x_1, x_2, \ldots, x_N\}$, where N is the number of super-pixels. The objective function of the FCM algorithm is defined by the following:

$$J_m(U, Z) = \sum_{j=1}^{N} \sum_{i=1}^{C} (u_{ij})^m (x_j - z_i)^2 \tag{7}$$

where C is the number of clusters, $x_j \in X$, m is the fuzzy weight index and the value of m is usually equal to 2, $u_{ij} \subseteq U$ is the membership of sample x_j belonging to class i, $u_{ij} \in [0, 1]$ and $\sum_{i=1}^{C} u_{ij} = 1$, $z_i \subseteq Z$ is the cluster center of class i.

In this iteration, the updates of u_{ij} and z_i are calculated using Formulas (8) and (9).

$$u_{i,j} = \frac{1}{\sum_{k=1}^{C} ((x_j - z_i)/(x_j - z_k))^{2/(m-1)}} \tag{8}$$

$$z_i = \sum_{j=1}^{N} (u_{i,j})^m x_j / \sum_{j=1}^{N} (u_{ij})^m \tag{9}$$

3.4. Fine Layover Detection

After the rough layover detection, Dense building areas (denoted as Den_{Build}) are preliminarily removed. However, small parts of the layover areas are treated as Dense building areas due to the super-pixel segmentation. One of the tasks of fine layover detection is to identify these layover areas in Den_{Build}. Meanwhile, $Spar_{Build}-Lay$ is a mixed area of layover and a Sparse building area, and the more important task of this stage is to separate the two.

The flowchart of this stage is shown as Figure 5. Farmland extraction obtains the image of farmland from the initial classification result, whose relationship with Sparse buildings is needed for detection. Additionally, the connected domains of farmland and the two results in the previous stage should be generated in the second step. Layover is the target of this detection, and every connected domain in mixed areas needs to be processed; therefore, any neighborhood set in farmland and Dense building areas should be prepared. The third step is used to calculate them. Then, the next three steps are key to processing fine detection, in which the spatial neighborhood relationship is the major criterion.

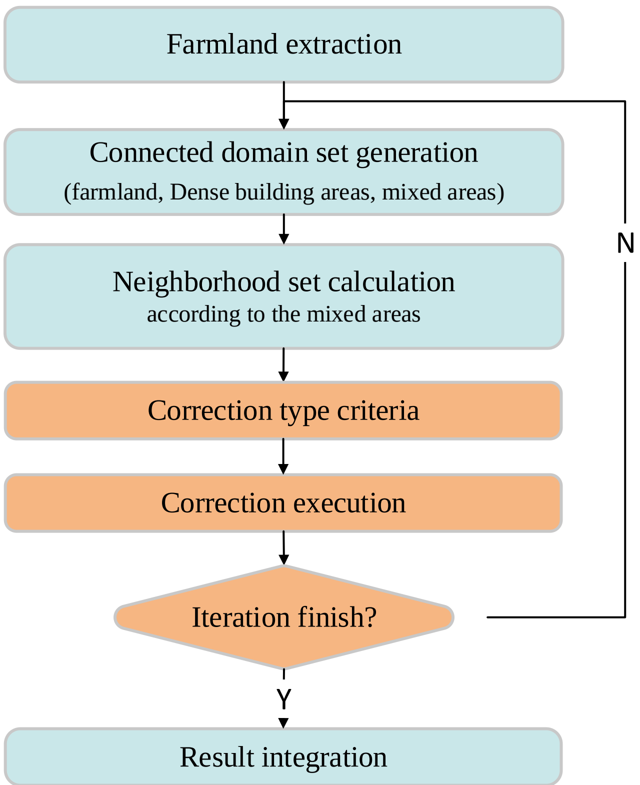

Figure 5. Flow chart of fine layover detection.

Suppose $Iniclas_{farm}$ is the result of farmland areas in $Iniclas$. L, B and F are the connected domain sets in $Spar_{Build}-Lay$, Den_{Build} and $Iniclas_{farm}$, respectively. The criteria of this stage are designed as follows:

$$S_{L_i} < \max(S_{NB_{L_i}}) \text{or} \max(S_{NF_{L_i}}) > P \tag{10}$$

where S represents the number of pixels in the connected domain; L_i represents the i-th connected domain of $Spar_{Build}-Lay$; and NB_{L_i} and NF_{L_i} represent the set of Dense building area and farmland area connected domains in the neighborhood of L_i, respectively. P is an empirical constant on the farmland scale. In general, its value is within the range 1–30,000 pixels. The experiments of specific study areas should be conducted for the optimal parameter.

When L_i conforms to Formula (10), L_i is identified as a Sparse building area, otherwise the area of NB_{L_i} is corrected to layover. When these amendments are completed iteratively, the complete layover areas will be generated, and the actual built-up areas, including Dense building and Sparse building areas, are also integrated.

4. Experimental Results and Analysis

4.1. Study Area and Data

The Danjiangkou Reservoir area ($110^{\circ}4'232''$ to $111^{\circ}57'44''$ E, $32^{\circ}12'11''$ to $33^{\circ}3'35''$ N) is the water source of the middle route of the South-to-North Water Transfer Project [33–36], which is the largest water resources distribution project in China. The project benefits more than 200 million people in 14 cities across 4 provinces. It is of great significance to be able to accurately investigate the land cover using SAR remote sensing technology for further ecological protection.

Figure 6 shows the location and images of the Danjiangkou Reservoir study area. As can be seen from Figure 6a, Shiyan City, Danjiangkou City and Laohekou City are all in this area, and there are dense buildings in these urban areas. Meanwhile, referring to Figure 6c, there is a large area of continuous mountains to the west and south of the study area, which causes more layover phenomena in the SAR image. Taking this area as the study area can verify the effectiveness of the proposed method.

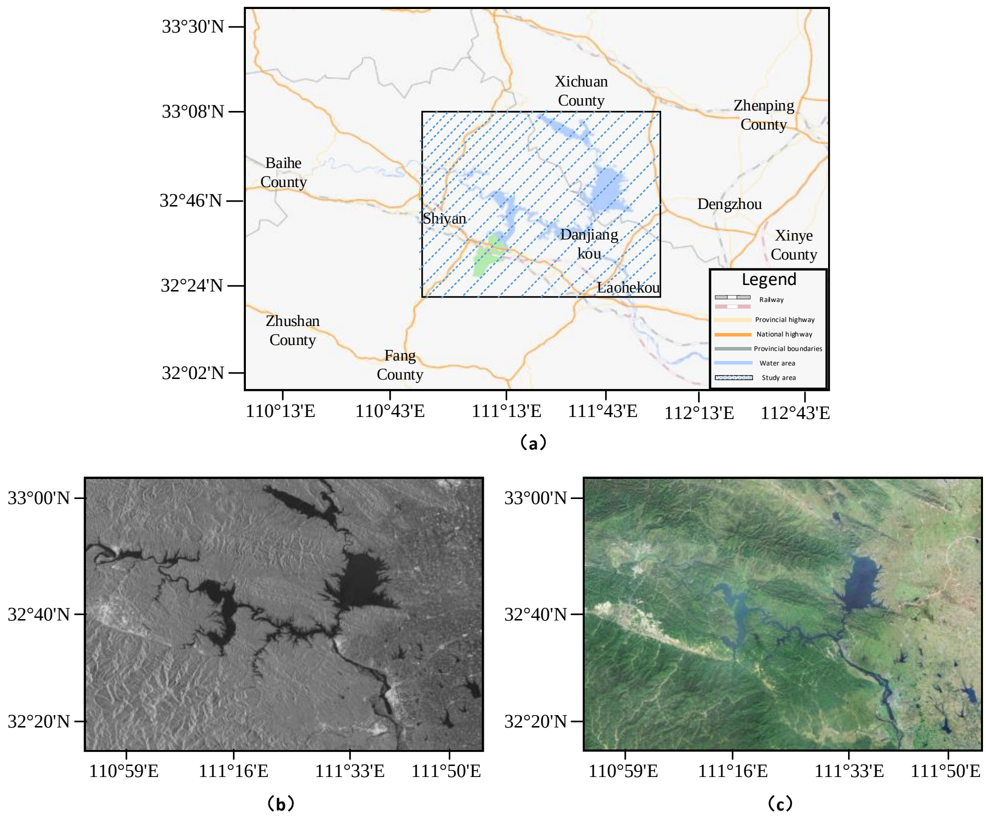

Figure 6. Location and images of study area: (**a**) location; (**b**) SAR image; (**c**) optical image.

Figure 6b is a SAR image of the study area from the Sentinel-1A satellite. The SAR sensor works in the C-band and can obtain two VV and VH polarization images in the interferometric wide-swath model [37]. The 31 SAR images used have a resolution of 5 m $\times$ 20 m (range and azimuth) and a swath width of 250 km; they are listed in Table 4.

Table 4. SAR images of the study area.

Study Area	Image Date
Danjiangkou Reservoir	1/May/2019, 13/May/2019, 6/June/2019, 18/June/2019, 30/June/2019, 12/July/2019, 24/July/2019, 5/August/2019, 17/August/2019, 29/August/2019, 10/September/2019, 22/September/2019, 4/October/2019, 16/October/2019, 28/October/2019, 9/September/2019, 21/November/2019, 3/December/2019, 15/December/2019, 27/December/2019, 8/January/2020, 20/January/2020, 1/February/2020, 13/February/2020, 25/February/2020, 8/March/2020, 20/March/2020, 1/April/2020, 13/April/2020, 25/April/2020, 7/May/2020

These SAR images should be preprocessed before being used, and the preprocessing includes multilook, co-registration, filtering, geocoding and radiometric calibration, as shown in Figure 7. The filtering method is refined Lee filtering with a 7 × 7 window.

Figure 7. Sentinel-1A SAR image preprocessing.

4.2. Layover Detection Experiment

There are four main land cover types, namely woodland, farmland, built-up areas and water, in the study area. A total of 31 SAR images were used to calculate the BC of each land cover type, including layover. The BC analyses of the VV and VH images were carried out according to the method mentioned in Section 2.2.

Figure 8 illustrates the change tendencies of BC with time series, and the values are basically consistent with those in Table 2. The built-up areas and layover areas have high BC values, but most of them are almost the same in the VH image, which is difficult to distinguish. For the sake of obtaining better detection results, one VV image should be selected for the initial recognition of ground objects.

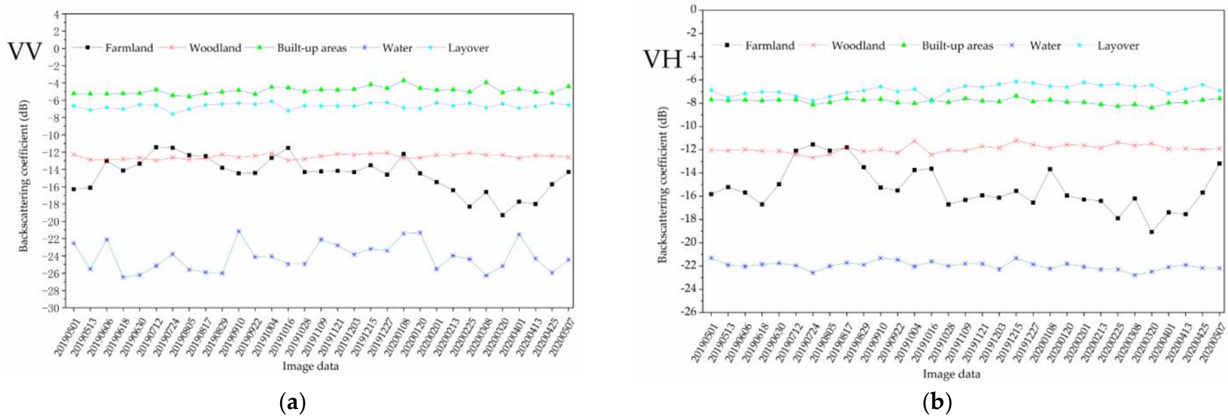

Figure 8. BC temporal tendencies of different objects: (**a**) that of VV images; (**b**) that of VH images.

The standard deviation of the BC of different ground objects for each VV image was calculated, and the values of the eight images acquired from 8 March to 25 April 2020 are higher than the others; they are all about 7.5. That is, any of these eight images could have been selected. Referring to prior knowledge of the land cover of the study area, the image of 25 April 2020 was selected to enter the subsequent detection stage. This image is 5140 × 7520 in size, covering an area of 15,461 square kilometers, as shown in Figure 9.

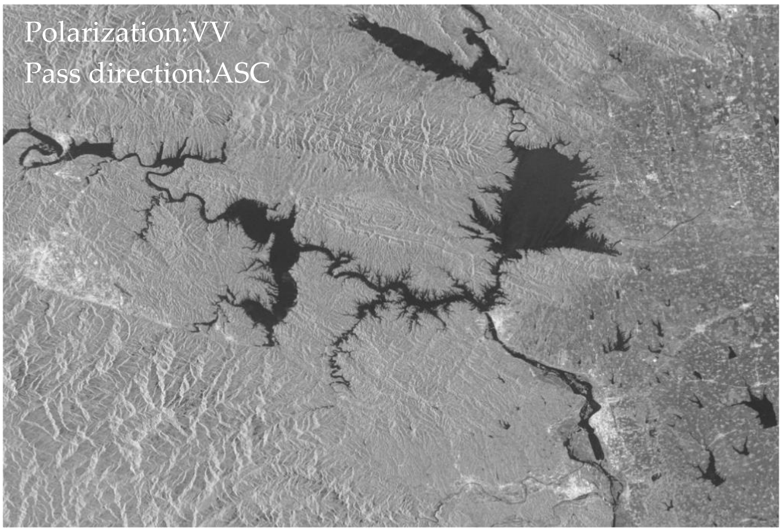

Figure 9. The selected SAR image for classification.

The classification result using the OGMRF-RC method is shown as Figure 10a. We expected many areas in the western and southern mountains to be classified as the built-up areas, marked with red in Figure 10a. Actually, these areas should be layover caused by the mountains. Figure 10b is the optical image of the same area. Observing the enlarged region marked with a black rectangle in the two images of Figure 10, it can be confirmed that there are no buildings, and the red patches in the west and south of Figure 10a are layover areas.

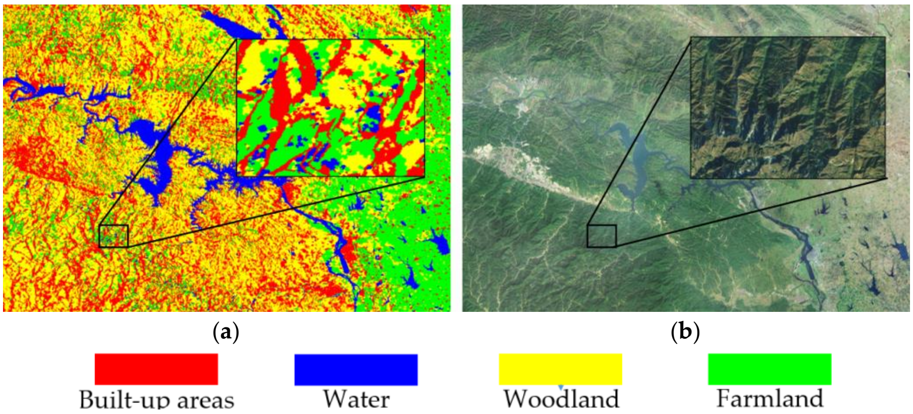

Figure 10. Comparison between the classification result and optical image: (**a**) classification result; (**b**) optical image.

Based on the classification result, the two images of the built-up areas could be extracted from the VV and VH image, as shown in Figure 11a,b. The difference image of them could be calculated, as shown in Figure 11c. Thus, the BC values of the Dense building areas were enhanced, and those of the Sparse building areas and layover areas were kept. As seen in Figure 11c, the Dense building areas marked by orange circles are more obvious, while the Sparse building areas and layover areas marked by red rectangles are not.

The two images in Figure 12 are the results of rough layover detection. Figure 12a contains all the Dense buildings areas that can be detected, as well as a small amount of layover areas with high BCs caused by noise. Additionally, Figure 12b is a mixed image revealing the layover areas and the Sparse building areas, which cannot be distinguished using a region-based FCM algorithm.

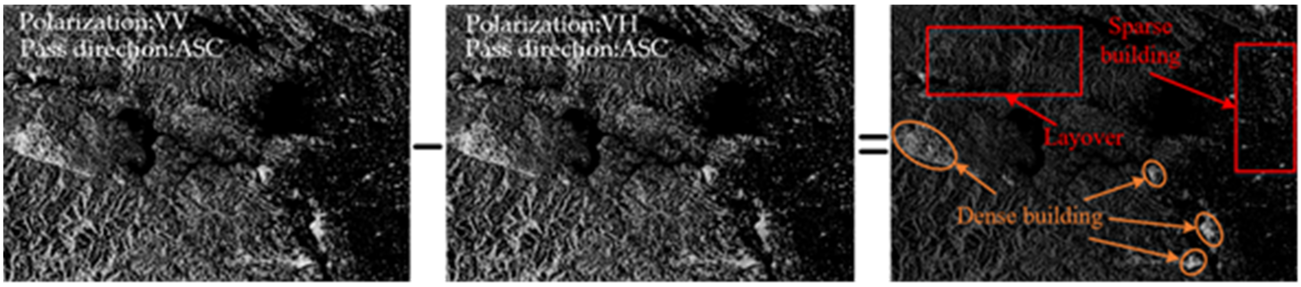

(**a**) (**b**) (**c**)

Figure 11. Generation process of difference image containing only built-up information: (**a**) VV image; (**b**) VH image; (**c**) |VV-VH| difference image.

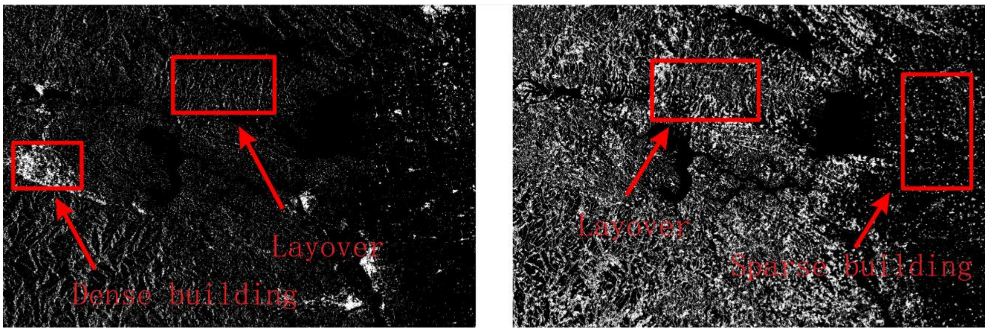

(**a**) (**b**)

Figure 12. Rough layover detection results: (**a**) layover and Dense building areas; (**b**) layover and Sparse building areas.

For the Danjiangkou Reservoir area, the analysis experiments of ground objects based on prior knowledge of land cover were carried out, and the optimal value of P in Formula (10) was set as 3000. The results of fine detection are shown in Figure 13. Figure 13a shows the final result of the layover areas, including the corresponding areas of Figure 12a,b. Additionally, Figure 13b shows the built-up areas, combining the Dense building areas and the Sparse building areas.

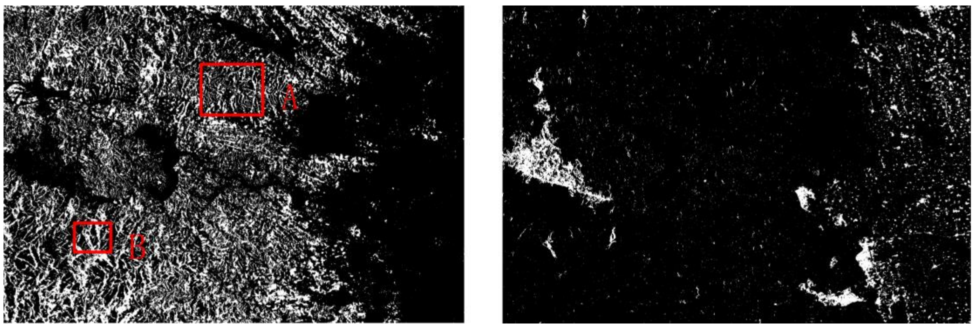

(**a**) (**b**)

Figure 13. Fine layover detection results: (**a**) layover areas; (**b**) built-up areas, including Dense building areas and Sparse building areas. Note: Region A and B are the selected regions for subsequent quantitative analysis.

4.3. Quantitative Analysis and Discussion

In order to better illustrate its applicability and effectiveness, comparison experiments were adopted to analyze the detection results. One experiment changed the study area with the proposed method to verify its universality, and another experiment selected a different detection method to compare the accuracy.

An aggregative indicator, figure of merit (*FoM*) [38] was introduced to evaluate the detection accuracy. Formula (11) is used to calculate the *FoM*, in which the statistical results about correct detection (layover and detected), missed detection (layover but undetected) and false detection (non-layover but detected) are used. *FoM* considers various possible results; therefore, it can more comprehensively measure the detection accuracy.

$$FoM = \frac{N_c}{N_c + N_M + N_{FA}} \times 100\frac{0}{0} \tag{11}$$

where N_c, N_M and N_{FA} represent the numbers of pixels correctly detected, missed and falsely detected, respectively.

4.3.1. Accuracy Analysis of the Proposed Method

Region A and Region B, marked with the red rectangles in Figure 13a, were selected for the accuracy verification; they are 981 × 801 pixels and 578 × 469 pixels in size, respectively. There are mainly mountains and there are a lot of layover areas in the SAR images. Figure 14 shows the enlarged view of the SAR images, optical images and detection results of the two regions. It can be seen that the layover areas detected using this method are basically consistent with the actual ground conditions. The proposed method has a good effect on layover detection.

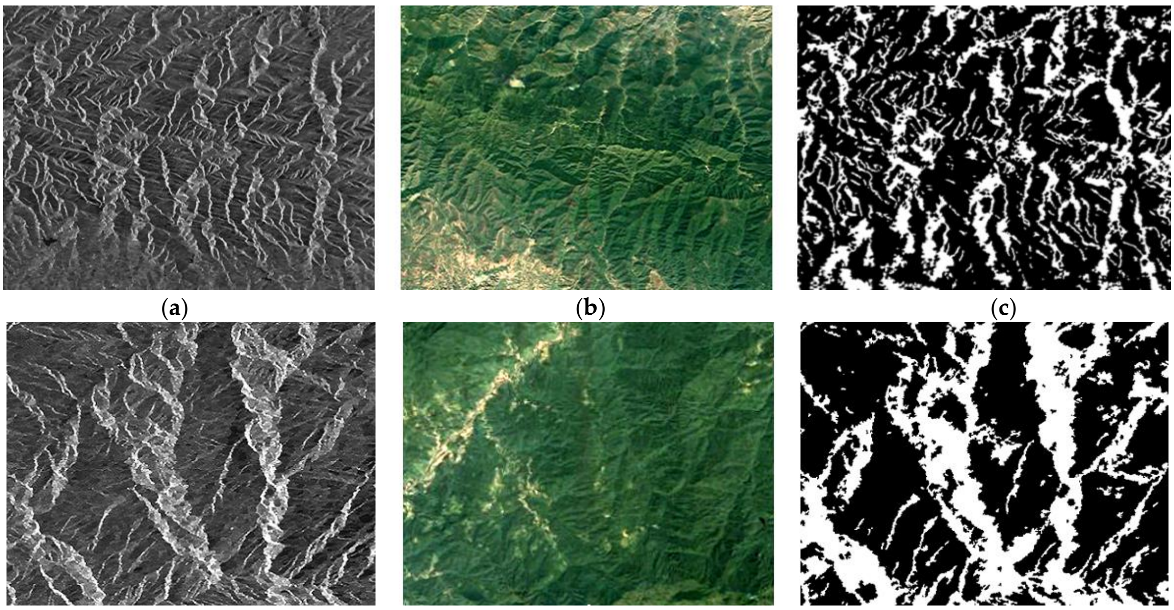

(**a**) (**b**) (**c**)
(**d**) (**e**) (**f**)

Figure 14. Comparison of two selected regions in Figure 13: (**a**–**c**) are the SAR image, optical image and the result of layover detection of region A; (**d**–**f**) are those of region B.

The quantitative evaluation was executed based on the manual processing. The actual layover areas were marked by visual interpretation, according to the comparison between the optical image and the SAR image. Then, the label results for correct detection, missed detection and false detection were obtained, as shown in Figure 15.

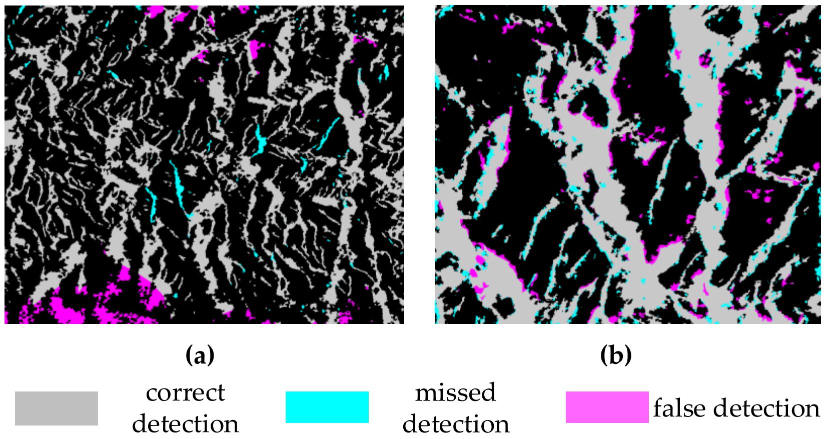

Figure 15. Label results of layover areas detected using the proposed method: (**a**) region A; (**b**) region B.

According to statistical analysis, the accuracies of the layover detection of Region A and Region B are shown in Table 5. Region A contains 192,762 pixels of layover in all, of which 185,307 pixels were correctly detected, 7455 pixels were missed and 18,839 pixels of other objects were wrongly detected as layover. The *FoM* calculated using Formula (11) reached 87.6%. Similarly, 88,541 of the 98,102 pixels of layover in Region B were correctly detected, 8167 pixels were missed and the *FoM* index was 83.3%.

Table 5. Detection accuracies of Region A and Region B.

	N_c	N_M	N_{FA}	*FoM*
Region A	185,307	7455	18,839	87.6%
Region B	88,541	9561	8167	83.3%

4.3.2. Universality Analysis of the Proposed Method

The proposed method is mainly aimed at the layover detection caused by undulating terrain such as mountains. The South Taihang area (112°20′4″ to 114°35′39″ E, 34°57′1″ to 36°18′35″ N) is an important ecological protection and restoration area in China. There is a wealth of woodland and mineral resources [36]. The removal of layover areas can effectively promote the monitoring application of SAR remote sensing in this area. Therefore, taking this area as the universality verification area has important practical significance. A SAR image and an optical image of South Taihang area are shown in Figure 16.

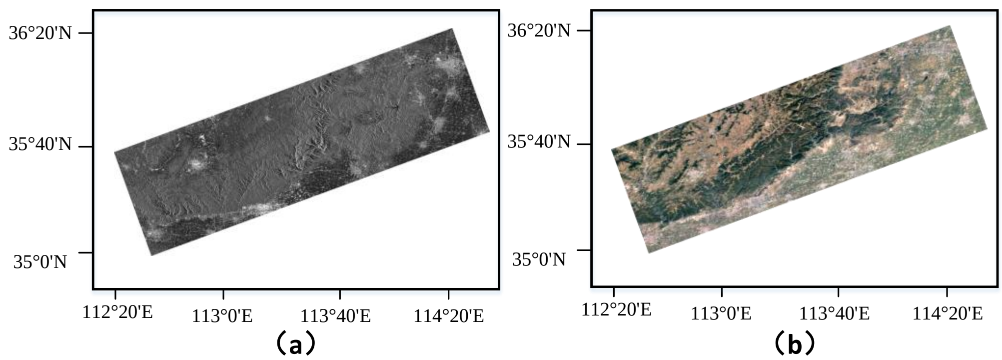

Figure 16. Images of South Taihang area: (**a**) SAR image; (**b**) optical image.

A total of 29 SAR images of the South Taihang area were collected, and these are listed in Table 6. Through the BC analysis of ground objects, the image taken on 20 April 2020 was selected, and its size is 8156 × 13,558, covering an area of 18,659 square kilometers.

Table 6. SAR images of South Taihang area used in this study.

Study Area	Image Date
South Taihang	19/July/2019, 31/July/2019, 12/August/2019, 24/August/2019, 5/September/2019, 17/September/2019, 29/September/2019, 11/October/2019, 23/October/2019, 4/November/2019, 16/November/2019, 28/November/2019, 10/December/2019, 22/December/2019, 3/January/2020, 15/January/2020, 27/January/2020, 8/February/2020, 3/March/2020, 15/March/2020, 27/March/2020, 8/April/2020, 20/April/2020, 2/May/2020, 14/May/2020, 7/June/2020, 19/June/2020, 1/July/2020, 25/July/2020

After the four stages of initial processing, difference image calculation and rough and fine layover detection, the distribution of layover areas was obtained, as shown in Figure 17. We enlarged Regions C and D marked in Figure 17, and compared the SAR image, optical image and detection results in Figure 18. The layover areas detected were highly consistent with the real ground situation.

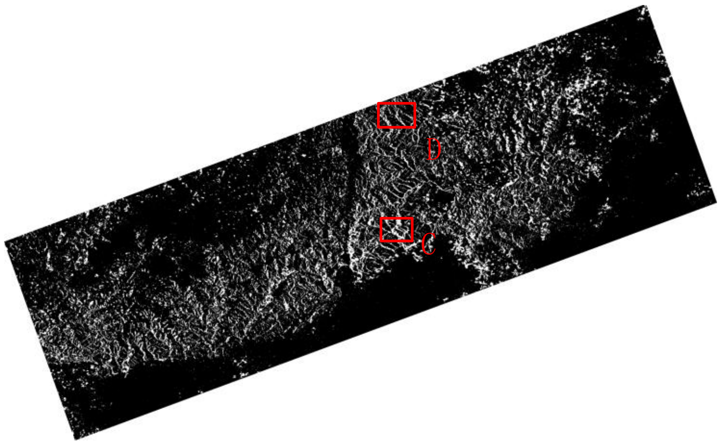

Figure 17. Layover detection results. Note: Region C and D are the selected regions for subsequent quantitative analysis.

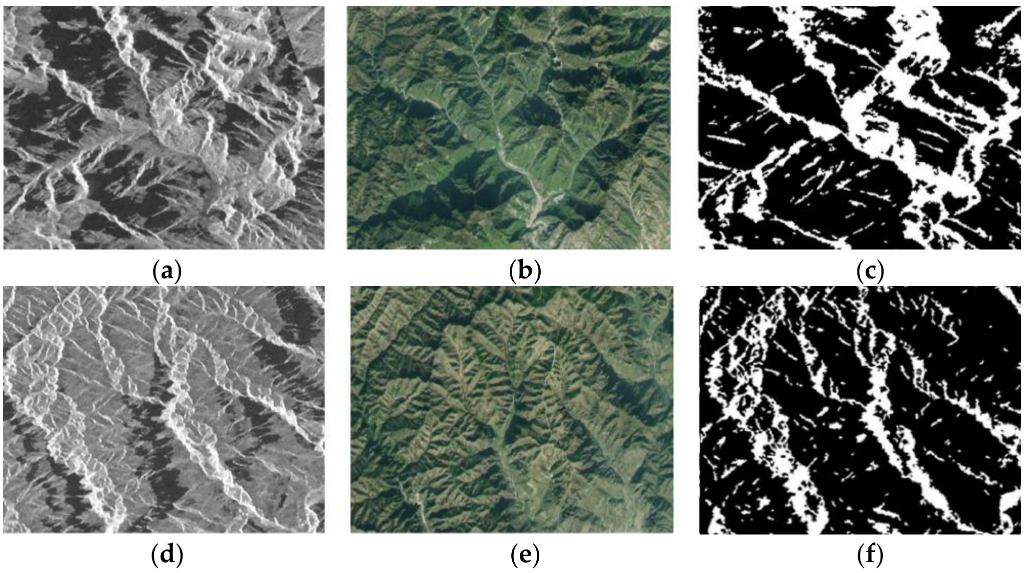

Figure 18. Comparison of two selected regions in Figure 17: (**a**–**c**) are the SAR image, optical image and the result of layover detection of region C; (**d**–**f**) are those of region D.

In the same way, the quantitative evaluations with the *FoM* of Region C and Region D were performed. The manual label results are shown in Figure 19, and the detection accuracies of Region C and Region D are shown in Table 7. The FoMs of the two regions are 86.0 and 85.6%, respectively.

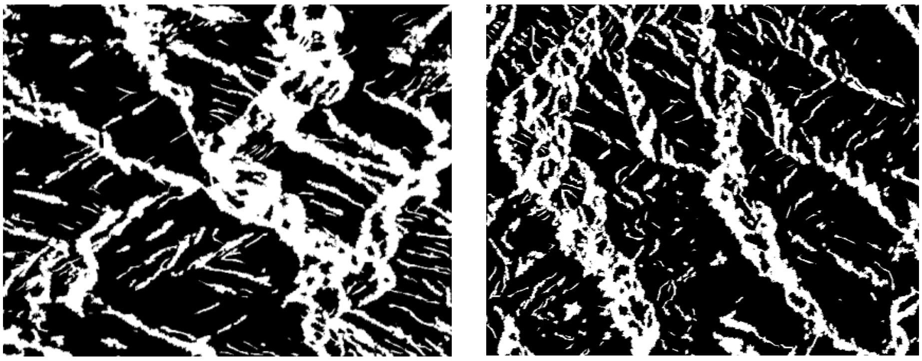

(a) (b)

Figure 19. Label results of layover areas detected using the proposed method: (**a**) Region C; (**b**) Region D.

Table 7. Detection accuracies of Region C and Region D.

	N_c	N_M	N_{FA}	*FoM*
Region C	84,594	5126	8640	86.0%
Region D	67,818	5110	6316	85.6%

In general, the accuracies of the layover detection of Danjiangkou Reservoir area and South Taihang area are all around 85%. This shows that this method is effective and suitable for layover detection in mountainous areas. Meanwhile, it does not require high-resolution SAR images and other auxiliary data. There will be more application space for this proposed method.

4.3.3. Comparative Analysis with Other Method

Considering the feasibility and effectiveness of the algorithm, the layover detection method mentioned in the literature [16] was reproduced as the comparative method in this study. The interference amplitude and correlation coefficient are the main basis of the method. By analyzing them, we found that the amplitude value of layover is generally higher, while the correlation coefficient is, conversely, lower than the normal value. In this method, the interference amplitude diagram and coherence coefficient diagram are calculated from SAR images at first, and then the threshold segmentation algorithm is used to recognize the layover area.

For consistency, the Danjiangkou Reservoir area was still taken as the study area, and two SAR images taken on 25 April 2020 and 7 May 2020 were adopted in this experiment. Due to the need for this method, the DEM data of the study area were also used. The result of layover detection is shown in Figure 20.

As can be seen from Figure 20, this comparative method can also detect most of the layover areas. It is worth noting that Region E and Region F marked in Figure 20 are built-up areas but were detected as layover areas. When Region E in the result images of our method and the comparative method is enlarged, as shown in Figure 21, the phenomenon can be seen obviously. The proposed method can accurately detect the layover areas caused by mountains and distinguish them from built-up areas well. This is useful for the SAR applications based on classification. For the comparative method, taking the built-up areas detected as layover areas into account, the overall accuracy will greatly reduce. Indeed, this is also a common problem in most of such methods.

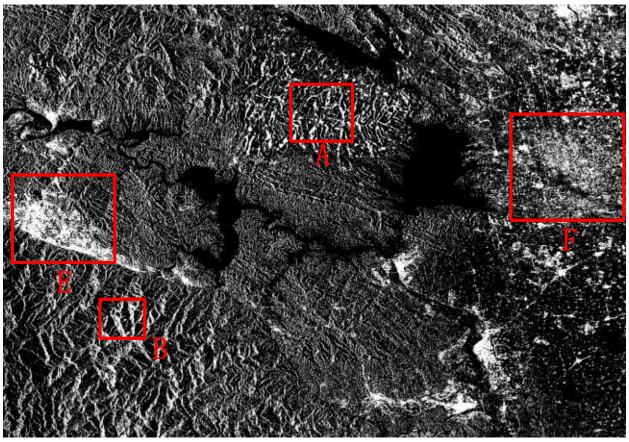

Figure 20. Layover detection result of the comparative method. Note: Region A, B, E and F are the selected regions for subsequent quantitative analysis.

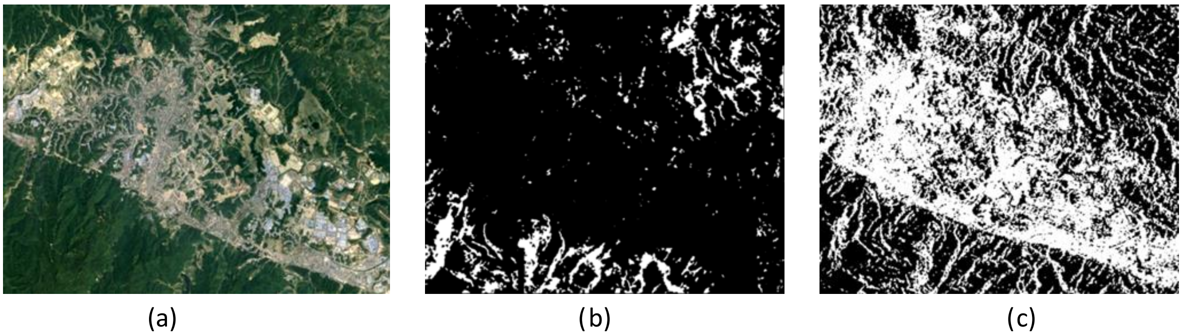

Figure 21. Comparison of detection results of Region E: (**a**) optical image; (**b**) result of the proposed method; (**c**) result of the comparative method.

When only considering layover areas in mountainous areas, Region A and Region B, in the same location as Figure 13, were still the areas of accuracy verification. Manual labeling of them was performed, as shown in Figure 22. Additionally, the detection accuracies are listed in Table 8. The number of pixels correctly detected using the two methods was roughly the same, whether in Region A or Region B. However, the number of pixels missed or falsely detected using our method was lower than that in the comparative method. Additionally, the index values of *FoM* are 81.1 and 75.1% in the two regions, respectively, which are at least six percentage points lower than those of our results.

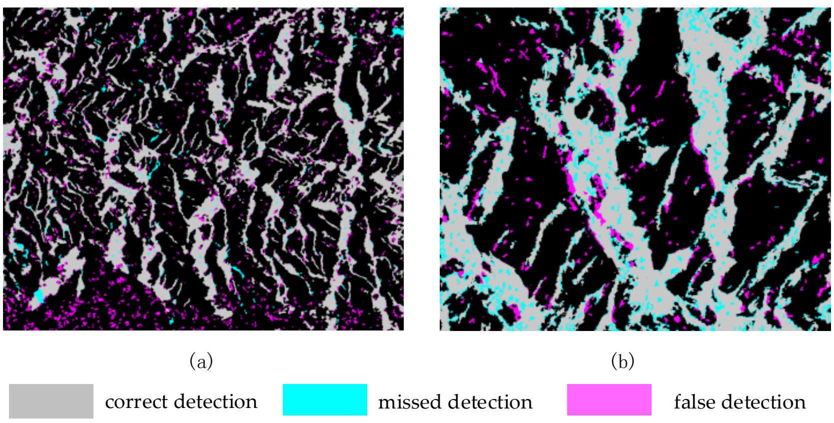

Figure 22. Label result of layover areas detected using the comparative method: (**a**) Region A; (**b**) Region B.

Table 8. Detection accuracies of the two regions of the comparison method.

	N_c	N_M	N_{FA}	*FoM*	$Difference_{FoM}$
Region A	182,166	10,596	31,732	81.1%	6.5% lower
Region B	80,730	17,372	9295	75.1%	8.2% lower

$Difference_{FoM}$ is the difference of *FoM* between the proposed method and the comparative method.

5. Conclusions

In this study, a simple and effective method on layover detection, fitted to mountainous areas, was introduced. This method is mainly based on the BC analysis of the different ground objects and different polarization modes with time series SAR images. An optimal image in VV mode was selected to perform the initial classification. Due to the similarity of BC, layover would be classified in the built-up areas. Considering the different densities and compositions of buildings in cities and suburbs, layover areas, Dense building areas and Sparse building areas were defined here. Additionally, the difference image of VV and VH images was calculated and segmented to remove most of the Dense building areas, and the spatial relationship between buildings and the surrounding ground objects was used in the fine detection of layover areas. Through multiple groups of comparative experiments, the detection accuracy of the proposed method was satisfactory, and the highest value of the *FoM* index was up to 87.6%. Meanwhile, simplicity is the evident advantage of this method, which only needs a single SAR image and does not require other auxiliary data.

In general, the proposed method has simple data requirements and a good execution effect for layover detection in mountainous areas. This means that most layover areas can be detected and removed from a SAR image in a similar environment, which will greatly broaden the application of SAR remote sensing. In the contemporary era, many regulatory works in mountainous areas need the support of SAR remote sensing technology, such as land surface surveys, ecological monitoring, environmental protection, etc. However, the layover phenomenon seriously affects the availability of SAR images. Using the proposed method to remove them, the above works would be completed well with the help of SAR remote sensing technologies.

Meanwhile, this method is not perfect, and improvement is necessary in the future. For example, an adaptive threshold could be generated to automatically fit different areas in the fine layover detection stage. Additionally, it is certain that the use of high-resolution SAR images will be helpful to enhance the detection accuracy when they become more popular.

Author Contributions: L.W. and Y.L. designed the study; L.W. and H.W. conducted the experiments, L.W., Z.G. and N.L. completed the analysis and wrote the manuscript; L.W., Y.L., Z.G. and N.L. contributed to discussions and revisions, providing important feedback and suggestions. All authors have read and agreed to the published version of the manuscript.

Funding: This research was funded by the National Natural Science Foundation of China (61871175); the College Key Research Project of Henan Province (21A520004); the Plan of Science and Technology of Henan Province (212102210093, 202102210175, 212102210101); and the Key Laboratory of Land Satellite Remote Sensing Application, Ministry of Natural Resources of the People's Republic of China (KLSMNR-202102).

Institutional Review Board Statement: Not applicable.

Informed Consent Statement: Not applicable.

Data Availability Statement: The Sentinel-1 SAR images used are provided free by the European Space Agency (ESA). The land cover data used are provided free by the Aerospace Information Research Institute (AIR).

Acknowledgments: Thanks to all the colleagues who have made efforts for this study and experiments.

Conflicts of Interest: The authors declare no conflict of interest.

References

1. Zhang, T.; Zhang, X. High-Speed Ship Detection in SAR Images Based on a Grid Convolutional Neural Network. *Remote Sens.* **2019**, *11*, 1206. [CrossRef]
2. Ghazifard, A.; Akbari, E.; Shirani, K.; Safaei, H. Evaluating land subsidence by field survey and D-InSAR technique in Damaneh City, Iran. *J. Arid. Land* **2017**, *9*, 778–789. [CrossRef]
3. Kang, M.; Baek, J. SAR Image Change Detection via Multiple-Window Processing with Structural Similarity. *Sensors* **2021**, *21*, 6645. [CrossRef] [PubMed]
4. Gao, Y.; Gao, F.; Dong, J.; Wang, S. Change Detection From Synthetic Aperture Radar Images Based on Channel Weighting-Based Deep Cascade Network. *IEEE J. Sel. Top. Appl. Earth Obs. Remote Sens.* **2019**, *12*, 4517–4529. [CrossRef]
5. Zhang, X.; Liu, G.; Zhang, C.; Atkinson, P.M.; Tan, X.; Jian, X.; Zhou, X.; Li, Y. Two-Phase Object-Based Deep Learning for Multi-Temporal SAR Image Change Detection. *Remote Sens.* **2020**, *12*, 548. [CrossRef]
6. Chen, H.; Shi, Z. A Spatial-Temporal Attention-Based Method and a New Dataset for Remote Sensing Image Change Detection. *Remote Sens.* **2020**, *12*, 1662. [CrossRef]
7. Doulgeris, A.P. An automatic u-distribution and markov random field segmentation algorithm for PolSAR images. *IEEE Trans. Geosci. Remote Sens.* **2014**, *53*, 1819–1827. [CrossRef]
8. Maghsoudi, Y.; Collins, M.J.; Leckie, D.G. Radarsat-2 Polarimetric SAR Data for Boreal Forest Classification Using SVM and a Wrapper Feature Selector. *IEEE J. Sel. Top. Appl. Earth Obs. Remote Sens.* **2013**, *6*, 1531–1538. [CrossRef]
9. De Oliveira, C.G.; Paradella, W.R. An Assessment of the Altimetric Information Derived from Spaceborne SAR (RADARSAT-1, SRTM3) and Optical (ASTER) Data for Cartographic Application in the Amazon Region. *Sensors* **2008**, *8*, 3819–3829. [CrossRef]
10. Miller, S.D.; Straka, W.C.; Bachmeier, A.S.; Schmit, T.J.; Partain, P.T.; Noh, Y.-J. Earth-viewing satellite perspectives on the Chelyabinsk meteor event. *Proc. Natl. Acad. Sci. USA* **2013**, *110*, 18092–18097. [CrossRef] [PubMed]
11. Yi, Y.S.; Zhang, L.R.; Xin, L.; Liu, N. A Large Scene Imaging Algorithm for Missile-borne Side-looking SAR. *J. Electron. Inf. Technol.* **2010**, *32*, 587–592. [CrossRef]
12. Gatelli, F.; Guamieri, A.M.; Parizzi, F.; Pasquali, P.; Prati, C.; Rocca, F. The wavenumber shift in SAR interferometry. *IEEE Trans. Geosci. Remote Sens.* **1994**, *32*, 855–865. [CrossRef]
13. Gini, F.; Lombardini, F.; Montanari, M. Layover solution in multibaseline SAR interferometry. *IEEE Trans. Aerosp. Electron. Syst.* **2002**, *38*, 1344–1356. [CrossRef]
14. Eineder, M.; Adam, N. A maximum-likelihood estimator to simultaneously unwrap, geocode, and fuse SAR interferograms from different viewing geometries into one digital elevation model. *IEEE Trans. Geosci. Remote Sens.* **2005**, *43*, 24–36. [CrossRef]
15. Cai, B.; Du, X.Y.; Dong, Z.; Liang, D.N. Layover and Shadow Detection Based on Distributed Spaceborne Single-Baseline InSAR. *J. Signal Process.* **2010**, *26*, 961–967. [CrossRef]
16. Ren, Y.; Zou, H.X.; Qin, X.X.; Ji, K.F. A method for layover and shadow detecting in InSAR. *J. Cent. South Univ.* **2013**, *44*, 396–400.
17. Du, X.Y.; Yang, Q.; Cai, B.; Liang, D.N. A new method on shadow and layover detection of InSAR. In Proceedings of the IEEE 2017 Sixth Asia-Pacific Conference on Antennas and Propagation (APCAP), Xi'an, China, 16–19 October 2017. [CrossRef]
18. Guindon, B.; Adair, M. Analytic Formulation of Spaceborne SAR Image Geocoding and "Value-Added" Product Generation Procedures using Digital Elevation Data. *Can. J. Remote Sens.* **1992**, *18*, 2–12. [CrossRef]
19. Li, N.; Wang, R.; Deng, Y.; Liu, Y.; Wang, C.; Balz, T.; Li, B. Polarimetric Response of Landslides at X-Band Following the Wenchuan Earthquake. *IEEE Geosci. Remote Sens. Lett.* **2014**, *11*, 1722–1726. [CrossRef]
20. Kakooei, M.; Nascetti, A.; Ban, Y. Sentinel-1 Global Coverage Foreshortening Mask Extraction: An Open Source Implementation Based on Google Earth Engine. In Proceedings of the IGARSS 2018—2018 IEEE International Geoscience and Remote Sensing Symposium, Valencia, Spain, 22–27 July 2018; pp. 6836–6839. [CrossRef]
21. Zhang, T.T.; Yang, H.L.; Li, D.M.; Li, Y.J.; Liu, J.N. Identification of layover and shadows regions in SAR images: Taking Badong as an example. *Bull. Surv. Mapp.* **2019**, *11*, 85–88. [CrossRef]
22. Wang, H.; Cheng, Q.; Wang, T.; Zhang, G.; Wang, Y.; Li, X.; Jiang, B. Layover Compensation Method for Regional Spaceborne SAR Imagery Without GCPs. *IEEE Trans. Geosci. Remote Sens.* **2021**, *59*, 8367–8381. [CrossRef]
23. Na, M.-A.; Gulnur, I.; Ma, C.-Y.; Mamat, S. Extraction of crop acreage based on multi-temporal and dual-polarization SAR data. *Acta Agron. Sin.* **2020**, *46*, 1099–1111. [CrossRef]
24. Xu, J.; Zhen, L.; Tian, B.S.; Lei, H.; Quan, C.; Fu, S.T. Polarimetric analysis of multi-temporal RADARSAT-2 SAR images for wheat monitoring and mapping. *Int. J. Remote Sens.* **2014**, *35*, 3840–3858. [CrossRef]
25. El Hajj, M.; Baghdadi, N.; Zribi, M.; Angelliaume, S. Analysis of Sentinel-1 Radiometric Stability and Quality for Land Surface Applications. *Remote Sens.* **2016**, *8*, 406. [CrossRef]
26. Yamaguchi, Y.; Sato, A.; Boerner, W.M.; Sato, R.; Yamada, H. Four-Component Scattering Power Decomposition With Rotation of Coherency Matrix. *IEEE Trans. Geosci. Remote Sens.* **2011**, *49*, 2251–2257. [CrossRef]
27. National Earth System Science Data Center. Available online: http://www.geodata.cn/ (accessed on 28 March 2021).
28. Zheng, C.; Yao, H. Segmentation for remote-sensing imagery using the object-based Gaussian-Markov random field model with region coefficients. *Int. J. Remote Sens.* **2019**, *40*, 4441–4472. [CrossRef]
29. Kumar, A.; Ghosh, S.K.; Dadhwal, V.K. Full fuzzy land cover mapping using remote sensing data based on fuzzy c-means and density estimation. *Can. J. Remote Sens.* **2007**, *32*, 81–87. [CrossRef]

30. Achanta, R.; Shaji, A.; Smith, K.; Lucchi, A.; Fua, P.; Süsstrunk, S. SLIC Superpixels Compared to State-of-the-Art Superpixel Methods. *IEEE Trans. Pattern Anal. Mach. Intell.* **2012**, *34*, 2274–2282. [CrossRef]
31. Zhang, Y.; Liu, K.; Dong, Y.; Wu, K.; Hu, X. Semisupervised Classification Based on SLIC Segmentation for Hyperspectral Image. *IEEE Geosci. Remote Sens. Lett.* **2019**, *17*, 1440–1444. [CrossRef]
32. Sun, W.; Guo, M. Image segmentation based on SLIC and conditional random field. *Appl. Res. Comput.* **2015**, *32*, 3817–3820. [CrossRef]
33. Tan, X.; Xia, X.; Li, S. Water quality characteristics and integrated assessment based on multistep correlation analysis in the Danjiangkou reservoir, China. *J. Environ. Inf.* **2015**, *25*, 60–70. [CrossRef]
34. Kang, L.; Xiaocong, H.E. Risk analysis of synchronous asynchronous encounter probability of rich-poor precipitation in the Middle Route of South-to-North Water. *J. Adv. Water Sci.* **2011**, *22*, 44–50. [CrossRef]
35. Wu, L.; Wang, L.; Min, L.; Hou, W.; Guo, Z.; Zhao, J.; Li, N. Discrimination of Algal-Bloom Using Spaceborne SAR Observations of Great Lakes in China. *Remote Sens.* **2018**, *10*, 767–789. [CrossRef]
36. Yu, Z.R.; Yang, X.M.; Chen, Y.J. Ecological protection and restoration of mountains-rivers-vegetations-farmlands-lakes-grasslands in Nantaihang area, Henan Province: Integrated landscape management. *Acta Ecol. Sin.* **2019**, *39*, 8886–8895. [CrossRef]
37. Geudtner, D.; Torres, R.; Snoeij, P.; Ostergaard, A.; Navas-Traver, I. Sentinel-1 mission capabilities and SAR system. In Proceedings of the 2013 IEEE Radar Conference, Ottawa, ON, Canada, 29 April–3 May 2013; pp. 1–4. [CrossRef]
38. Cui, X.C.; Su, Y.; Chen, S.W. Polarimetric SAR ship detection based on polarimetric rotation domain features and superpixel technique. *J. Radars* **2021**, *10*, 35–48.